Oxidation of the Sulfide Ligands to SO_4^{2-} in the Dinuclear Complex $\{RuCl[P(OMe)_3]_2\}_2(\mu\text{-}S_2)(\mu\text{-}Cl)(\mu\text{-}N_2H_4)$: Synthesis and Characterization of $\{RuCl[P(OMe)_3]_2\}_2(\mu\text{-}S_2)(\mu\text{-}Cl)(\mu\text{-}N_2H_4)^+HSO_4^-$, $\{RuCl_2[P(OMe)_3]_2\}_2(\mu\text{-}S)(\mu\text{-}N_2H_4)$, and $\{RuCl[P(OMe)_3]_2\}_2(\mu\text{-}S_2O_5)(\mu\text{-}N_2H_4)$

Kazuko Matsumoto,*,† Tetsuya Koyama,† and Yoshihiro Koide‡

Contribution from the Department of Chemistry and Advanced Research Center for Science and Engineering, Waseda University, Tokyo 169-8555, Japan, and Japan Science and Technology Corporation, Saitama 332-0012, Japan

Abstract: The paramagnetic dinuclear $Ru^{2+}Ru^{3+}$ complex, $\{RuCl[P(OMe)_3]_2\}_2(\mu\text{-}S_2)(\mu\text{-}Cl)(\mu\text{-}N_2H_4)$ (**1**), reduces dioxygen by one-electron at room temperature in CH_3CN to form $\mathbf{1}^+O_2^-$, in which O_2^- is coordinated to the $\mu\text{-}S_2$ ligand. The dioxygen reduction is preceded by protonation to yield HO_2^+ by the bridging hydrazine ligand. Complex **1** is electrochemically more negative than HO_2^+, and a redox reaction generates $\mathbf{1}^+$ and HO_2 ($\rightarrow O_2^- + H^+$). Spectroscopic studies (NMR and UV−vis) show that **1** and $\mathbf{1}^+O_2^-$ are under equilibrium, and the succeeding disproportionation reaction of $\mathbf{1}^+O_2^-$ produces two intermediates, $\mathbf{1}^+$ and the dithionite complex, $\mathbf{1}^+(O_2^-)_2$, as an intermediate. The dithionite intermediate undergoes Cl^- dissociation and further oxidation to yield the dinuclear Ru complex $\{Ru^{2+}Cl[P(OMe)_3]_2\}_2(\mu\text{-}S_2O_5)(\mu\text{-}N_2H_4)$ (**3**). The liberated Cl^- attacks the dithionite complex, and induces SO_4^{2-} dissociation to prepare the dinuclear complex $\{Ru^{3+}Cl_2[P(OMe)_3]_2\}_2\text{-}(\mu\text{-}S)(\mu\text{-}N_2H_4)$ (**5**). On the other hand, intermediate $\mathbf{1}^+$ forms an ion pair with HSO_4^-, which stems from the liberated SO_4^{2-}, to yield $[\{Ru^{3+}Cl[P(OMe)_3]_2\}_2(\mu\text{-}S_2)(\mu\text{-}Cl)(\mu\text{-}N_2H_4)]^+HSO_4^-$ (**4** = $\mathbf{1}^+HSO_4^-$). A trace of $\{Ru^{3+}Cl[P(OMe)_3]_2\}_2(\mu\text{-}S_2)(\mu\text{-}Cl)_2$ (**2**) is also detected in the supernatant. The UV−vis spectroscopic study revealed that complexes **2−5** are the exclusive products and the oxidation reaction can be balanced as follows: $14 \times \mathbf{1} + 4.5\ O_2 = \mathbf{2} + 5 \times \mathbf{3} + 4 \times \mathbf{4} + 4 \times \mathbf{5}$. The $^{18}O_2/^{16}O_2$ mixed-labeled oxygen studies proved that the external oxygen was the source of oxygen for the formation of the S_2O_5 and HSO_4^- groups in **3** and **4**, respectively. The structures of **3**, **4**, and **5** are characterized by X-ray crystallographic structure determinations. The dinuclear framework of complex **4** remains identical with that of **1** except for the significantly shorter Ru−S distance. The hydrazine hydrogens of complex **3** show intramolecular hydrogen bonding, which is reflected on a significantly low field shift of the hydrazine ^1H NMR resonance. Complex **3** possesses the $\mu\text{-}S_2O_5^{2-}$ ligand, in which the two $\mu\text{-}SO_2\text{-}O,S'$ bridges are linked at the sulfur atoms through the μ-oxo bonds. Comparison of the site symmetries around the Ru atoms of **1**, **3**, and **5** strongly supports the occurrence of coordination rearrangements.

Introduction

We have been investigating coordination chemistry and redox properties of the sulfide-bridged multinuclear ruthenium complexes, and demonstrated various chemistries by taking advantage of coordination flexibility of the $\mu\text{-}S_n^{2-}$ ($1 \leq n \leq 6$) bridge and robustness of the RuS_nRu framework.[1] A wide-spread use of S_n^{2-} ($n = 1$ or 2) in redox-active centers of metalloproteins[2] and ligands of numerous transition metal complexes[3] invokes coordination flexibility of the sulfur ligands. The RuS_nRu framework may provide a niche for activation of small molecules by electrochemistry,[4] photoexcitation,[5] and so on.[6] For example, dioxygen may be activated to oxidize the $\mu\text{-}S_n$ ligand,[7] subsequently generating sulfoxides and sulfuric acids.

Development of an artificial catalyst system for sulfur degradation of coal and crude oil is of great importance in apparent association with environmental concerns. Recently, biocatalytic degradation of organic sulfur has been actively investigated in expectation of replacing conventional hydrogenation processes. Dibenzothiophene monooxygenase (DszC) is one such example that oxidizes the sulfur atom in dibenzothiophene

* Address all correspondence to this author at Waseda University.
† Department of Chemistry and Advanced Research Center for Science and Engineering.
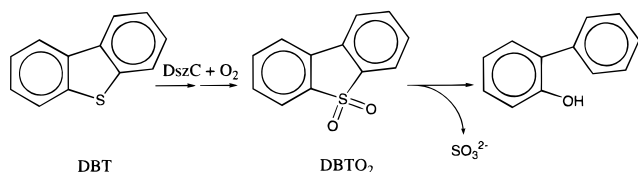‡ Japan Science and Technology Corporation.

(1) (a) Furuhashi, T.; Kawano, M.; Koide, Y.; Somazawa, R.; Matsumoto, K. *Inorg. Chem.* **1999**, *38*, 109. (b) Matsumoto, K.; Sano, Y. *Inorg. Chem.* **1997**, *36*, 4405. (c) *Transition Metal Sulfur Chemistry: Biological and Industrial Significance*; Stiefel, E., Matsumoto, K., Eds.; ACS Symp. Ser. No. 653; American Chemical Society: Washington, DC, 1996; Chapter 15. (d) Matsumoto, K.; Matsumoto, T.; Kawano, M.; Ohnuki, H.; Shichi, Y.; Nishide, T.; Sato, T. *J. Am. Chem. Soc.* **1996**, *118*, 3597. (e) Matsumoto, K.; Ohnuki, H.; Kawano, M. *Inorg. Chem.* **1995**, *34*, 3838. (f) Matsumoto, K.; Uemura, H.; Kawano, M. *Chem. Lett.* **1994**, 1215. (g) Kawano, M.; Uemura, H.; Watanabe, T.; Matsumoto, K. *J. Am. Chem. Soc.* **1993**, *115*, 2068. (h) Kawano, M.; Hoshino, C.; Matsumoto, K. *Inorg. Chem.* **1992**, *31*, 5158. (i) Uemura, H.; Kawano, M.; Watanabe, T.; Matsumoto, T.; Matsumoto, K. *Inorg. Chem.* **1992**, *31*, 5137. (j) Kawano, M.; Watanabe, T.; Matsumoto, K. *Chem. Lett.* **1992**, 2389. (k) Matsumoto, T.; Matsumoto, K. *Chem. Lett.* **1992**, 1539. (l) Matsumoto, T.; Matsumoto, K. *Chem. Lett.* **1992**, 559. (m) Matsumoto, T.; Matsumoto, K.; Sato, T. *Inorg. Chim. Acta* **1992**, *202*, 31.

10914 *J. Am. Chem. Soc., Vol. 121, No. 47, 1999*

Matsumoto et al.

Scheme 1

(DBT) to DBTO$_2$, and leads to eventual desulfurization as SO$_3^{2-}$ in the presence of oxygen (Scheme 1).[8]

Activation of the metal-coordinated ligands can be a useful method to mimic biocatalytic activities.[9] Although there is precedence for the oxidation of a metal-coordinated SO$_2$ to HSO$_4^{2-}$ using iron complexes,[10] ruthenium had attracted little attention until Mingos et al. employed the mononuclear ruthenium complex, RuH$_2$(PPh$_3$)$_4$.[11] When we set out to investigate the oxidation reaction using the disulfide-bridged Ru dimers prepared in our group, it was found that an CH$_3$CN solution of {RuCl[P(OMe)$_3$]$_2$}$_2$(μ-S$_2$)(μ-Cl)(μ-N$_2$H$_4$) (**1**) changed its color over days in the presence of oxygen. The resulting solution exhibited a surprisingly simple ^{31}P NMR spectrum, which prompted us to further identify the oxidation products. The oxidation reaction turned out to yield as many as three isolable products, among them the Ru dimer that forms a complex ion with HSO$_4^-$, which is produced by the oxidation of the μ-S$_2^{2-}$ bridge. Given that commercial production of SO$_4^{2-}$ starts from combustion of H$_2$S or elemental sulfur,[12] the oxidation reaction in this work occurs under incomparably mild condition. We also found that one of the products possesses an unprecedented μ-S$_2$O$_5^{2-}$-*O,S':O',S* ligand. In this report, the oxidation reaction of **1** is thoroughly studied by NMR, UV–vis spectroscopy, and ^{18}O-isotope labeling as well as X-ray crystallography.

(2) (a) Holm, R. H.; Simhon, E. D. In *Molybdenum Enzymes*; Spiro, T. G., Ed.; Wiley-Interscience: New York, 1985; Chapter 1. (b) Palermo, R. E.; Singh, R.; Bashkin, J. K.; Holm, R. H. *J. Am. Chem. Soc.* **1984**, *106*, 2600. (c) *Sulfur: Its Significance for Chemistry, for the Geo-, Bio- and Cosmosphere and Technology*; Müller, A., Krebs, B., Eds.; Elsevier: New York, 1984. (d) Holm, R. H. *Chem. Soc. Rev.* **1981**, *10*, 455. (e) Coucouvanis, D. *Acc. Chem. Res.* **1981**, *14*, 201. (f) Zumft, W. G. *Eur. J. Biochem.* **1978**, *91*, 345.

(3) (a) Müller, A.; Jaegermann, W.; Enemark, J. H. *Coord. Chem. Rev.* **1982**, *46*, 245. (b) Müller, A.; Dieman, E. In *Comprehensive Coordination Chemistry*; Wilkinson, G., Gillard, R. D., McCleverty, J. A., Eds.; Pergamon: Oxford, 1987; Vol. 2, p 541.

(4) Abruna, H. D.; Walsh, J. L.; Meyer, T. J.; Murray, R. W. *J. Am. Chem. Soc.* **1980**, *102*, 3272.

(5) Connick, W. B.; Gray, H. B. *J. Am. Chem. Soc.* **1997**, *119*, 11620.

(6) Valentine, A. M.; Lippard, S. J. *J. Chem. Soc., Dalton Trans.* **1997**, 3925.

(7) (a) Wang, R.; Mashuta, M. S.; Richardson, J. F.; Noble, M. E. *Inorg. Chem.* **1996**, *35*, 3022. (b) Farmer, P. J.; Reibenspies, J. H.; Lindahl, P. A.; Darensbourg, M. Y. *J. Am. Chem. Soc.* **1993**, *115*, 4665. (c) Lorenz, I.-P.; Messelhäuser, J.; Hiller, W.; Hang, K. *Angew. Chem., Int. Ed. Engl.* **1985**, *24*, 228.

(8) (a) Gray, K. A.; Pogrebinsky, O. S.; Mrachko, G. T.; Xi, L.; Monticello, D. J.; Squires, C, H. *Nature Biotechnol.* **1996**, *14*, 1705. (b) Ohshiro, T.; Hirata, T.; Izumi, Y. *Appl. Microbiol. Biotechnol.* **1995**, *44*, 249.

(9) See for example: (a) Grapperhaus, C. A.; Darensbourg, M. Y.; Sumner, L. W.; Russell, D. H. *J. Am. Chem. Soc.* **1996**, *118*, 1791. (b) Mizra, S. A.; Pressler, M. A.; Kumar, M.; Day, R. O.; Maroney, M. J. *Inorg. Chem.* **1993**, *32*, 977. (c) Shin, W.; Lindahl, P. A. *Biochim. Biophys. Acta* **1993**, *1161*, 317. (d) Schrauzer, G. N.; Zhang. C.; Chadha, R. *Inorg. Chem.* **1990**, *29*, 4104.

(10) (a) Beagley, B.; Kelly, D. G.; MacRory, P. P.; McAuliffe, C. A.; Pritchard, R. G. *J. Chem. Soc., Dalton Trans.* **1990**, 2657. (b) Scheidt, W. R.; Lee, Y. J.; Finnegan, M. G. *Inorg. Chem.* **1988**, *27*, 4725.
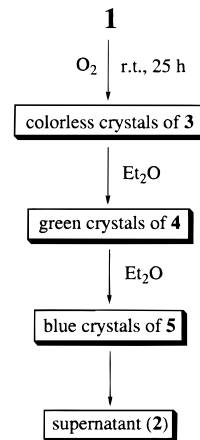
(11) Ghatak, I.; Mingos, D. M. P.; Hursthouse, M. B.; Abdul Malik, K. M. *Transiton Met. Chem.* **1979**, *4*, 260.

(12) Brändle, K. *Sulfur: Studies in Inorganic Chemistry*; Elsevier: New York, 1984; Vol. 5, p 237.

Scheme 2

R = OMe
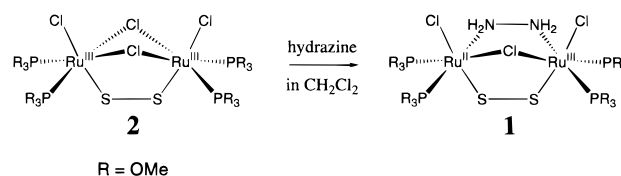
Scheme 3

Results and Discussion

Oxidation of {RuCl[P(OMe)$_3$]$_2$}$_2$(μ-S$_2$)(μ-Cl)(μ-N$_2$H$_4$) (1) in Acetonitrile. Among a number of dinuclear ruthenium complexes prepared in our research group,[1] complex **1** was obtained in the reaction of the dinuclear Ru^{3+}Ru^{3+} complex, {RuCl[P(OMe)$_3$]$_2$}$_2$(μ-S$_2$)(μ-Cl)$_2$ (**2**), with 2.25 equiv of hydrazine in CH$_2$Cl$_2$ (Scheme 2).[1h] The ESR studies revealed that complex **1** is paramagnetic and is better described as a valence-averaged Ru$^{2.5+}$Ru$^{2.5+}$ species.[1h] The oxidation reaction was conducted at room temperature by applying slightly negative pressure to a flask that contained a reddish-brown CH$_3$CN solution of **1**, and then was refilled with oxygen. In less than 25 h, the solution turned blue-green, a typical color for the sulfide-bridged Ru dimers.[1d] To our surprise, however, the solution yielded X-ray quality colorless crystals of {Ru^{2+}Cl-[P(OMe)$_3$]$_2$}$_2$(μ-S$_2$O$_5$)(μ-N$_2$H$_4$) (**3**), which was isolated by filtration (Scheme 3). After about half of the solvent was removed from the blue-green filtrate under reduced pressure, slow diffusion of diethyl ether yielded the green crystals of [{Ru^{3+}Cl[P(OMe)$_3$]$_2$}$_2$(μ-S$_2$)(μ-Cl)(μ-N$_2$H$_4$)]$^+$HSO$_4^-$ (**4**). Following the isolation of **4**, further condensation of the blue filtrate and subsequent dispersion of diethyl ether prepared the blue crystals of {Ru^{3+}Cl$_2$[P(OMe)$_3$]$_2$}$_2$(μ-S)(μ-N$_2$H$_4$) (**5**). A trace of complex **2** was detected in the supernatant.

XPS Study of 3. The oxidation states of the Ru atoms in complex **3** were determined by X-ray photoelectron spectroscopy (XPS). Previously we reported that the binding energies (B.E.) of Ru 3d$_{5/2}$ in several disulfide-bridged dinuclear Ru^{3+}-Ru^{3+} and Ru^{2+}Ru^{2+} complexes fall in the range of an experimental error (281.0–281.4 eV with fwhm 1.3–2.0 eV),[1d] and cannot be a probe for the Ru oxidation state. Complex **3** is no exception (B.E.{Ru 3d$_{5/2}$} = 281.0 eV (fwhm 1.7 eV)), precluding direct determination of the oxidation state. However, the B.E. of the sulfur atoms exhibit clear dependence on the oxidation state: 168.6–169.5 eV/SO$_4^{2-}$, 167.3–168.5 eV/HSO$_4^-$, 167.2–167.5 eV/SO$_3^{2-}$, 161.7–162.5 eV/S*SO$_3^{2-}$ (*
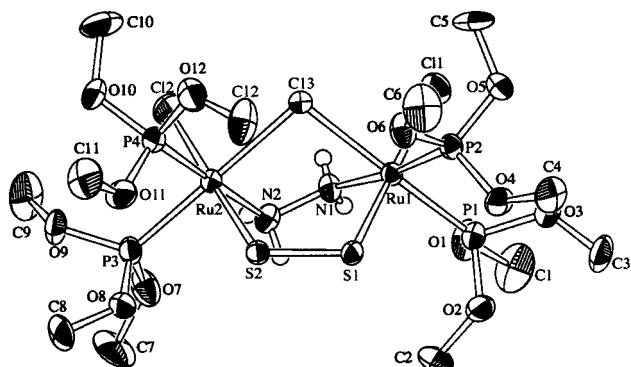
Figure 1. ORTEP diagram of [{RuCl[P(OMe)$_3$]$_2$}$_2$(μ-S$_2$)(μ-Cl)(μ-N$_2$H$_4$)]$^+$HSO$_4^-$ (**4**) showing 50% probability thermal ellipsoids for all non-hydrogen atoms.

for the observed atom), 167.7 eV/SS*O$_3^{2-}$, and 167.4 eV/SO$_2$.[13] Therefore, from the B.E. of S$_2$O$_5$ (167.3 eV) in **3**, +4 charge is assigned to the sulfur atoms. Consequently, the S$_2$O$_5$ group must possess net charge of -2 that imposes +2 charge on the Ru atoms.

Structural Characterization of [{RuCl[P(OMe)$_3$]$_2$}$_2$(μ-S$_2$)-(μ-Cl)(μ-N$_2$H$_4$)]$^+$HSO$_4^-$ (4). The crystallographic structure of complex **4** closely resembles that of **1** except for the existence of HSO$_4^-$, which is bound to the complex molecule via hydrogen bonds. Therefore, complex **4** can be alternatively written as **1**$^+$HSO$_4^-$. The crystal structure of **4**, along with the atom-labeling scheme, and the hydrogen bonding scheme are shown in Figures 1 and 2, respectively. Selected bond distances and angles are listed in Table 1. The Ru–S distances in the sulfur-bridged Ru dimers usually show apparent dependence on the metal oxidation states,[1d] and the distance is shorter for Ru^{3+} than for Ru^{2+}. In complex **4**, the oxidation resulted in considerable shortening of the Ru–S distances (2.191(2) and 2.204(2) Å) compared to those values in **1** (2.266(2) and 2.296-(2) Å), and now they are comparable to those found in complex **2** (2.198(3) and 2.205(5) Å). This is presumably due to depletion of the electron density of the π antibonding orbital localized in the Ru$_2$S$_2$ core.[1d,h] Selected bond distances and angles of **1** and **4** are compared in Table 2. The packing diagram shows that two HSO$_4^-$ anions are entwined around the inversion center, bound via two O–H···O contacts (Figure 2), and the twin moiety is further bound to two complex molecules. One long (1.581(7) Å) and three short (1.431(8), 1.437(8), and 1.465(7) Å) S–O bonds in HSO$_4^-$ correspond to an S–OH$^-$ single bond and S=O double bonds, respectively. The three S=O oxygens are bound to the hydrazine ligands via O···HN$_{hydrazine}$ contacts, in which two of them are bound to one **1**$^+$, and the third one to the other **1**$^+$. The μ-N$_2$H$_4$ group is bound intramolecularly to O$_{OMe}$ and, unlike **1**, no longer has direct contact between the complex molecules.[1h]

Structural Characterization of {RuCl$_2$[P(OMe)$_3$]$_2$}$_2$(μ-S)-(μ-N$_2$H$_4$) (5). Complex **5** crystallizes in two visibly different shapes from CH$_2$Cl$_2$/diethyl ether, one as a needle and the other as a parallelepiped crystal. Both crystals were subjected to X-ray structural determination, and acetonitrile was found in the lattice of the parallelepiped crystal, {RuCl$_2$[P(OMe)$_3$]$_2$}$_2$(μ-S)(μ-N$_2$H$_4$)(**5**)·CH$_3$CN, whereas the needle crystal has no solvent molecule. Data of the nonsolvate crystal were used for structural refinement and the resulting ORTEP diagram is shown in Figure 3, along with the atom-labeling scheme. Selected bond distances
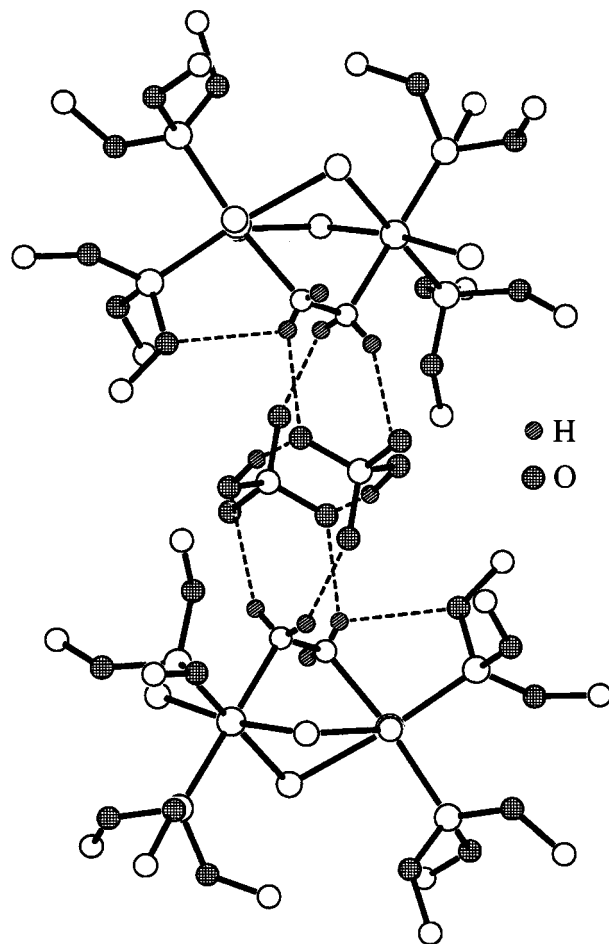
(13) Moulder, J. F.; Stickle, W. F.; Sobol, P. E.; Bomben, K. D. *Handbook of X-ray Photoelectron Spectroscopy*; Perkin-Elmer Co.: Edin Prairie, 1992; p 235.

Figure 2. Hydrogen bond interactions of **4**.

Table 1. Selected Bond Distances (Å) and Angles (deg) for **4**[a,b]

Bond Distances			
Ru(1)–Cl(1)	2.413(3)	Ru(1)–Cl(3)	2.463(2)
Ru(1)–S(1)	2.204(2)	Ru(1)–P(1)	2.237(2)
Ru(1)–P(2)	2.269(3)	Ru(1)–N(1)	2.175(9)
Ru(2)–Cl(2)	2.407(3)	Ru(2)–Cl(3)	2.486(2)
Ru(2)–S(2)	2.191(2)	Ru(2)–P(3)	2.225(3)
Ru(2)–P(4)	2.257(3)	Ru(2)–N(2)	2.210(8)
S(1)–S(2)	1.968(3)	N(1)–N(2)	1.45(1)

Bond Angles			
Cl(1)–Ru(1)–Cl(3)	88.14(8)	Cl(1)–Ru(1)–S(1)	179.42(10)
Cl(1)–Ru(1)–P(1)	87.04(9)	Cl(1)–Ru(1)–P(2)	94.03(10)
Cl(1)–Ru(1)–N(1)	82.5(2)	Cl(3)–Ru(1)–S(1)	92.35(8)
Cl(3)–Ru(1)–P(1)	172.72(9)	Cl(3)–Ru(1)–P(2)	94.61(8)
Cl(3)–Ru(1)–N(1)	78.7(2)	S(1)–Ru(1)–P(1)	92.44(9)
S(1)–Ru(1)–P(2)	86.23(9)	S(1)–Ru(1)–N(1)	97.3(2)
P(1)–Ru(1)–P(2)	91.17(9)	P(1)–Ru(1)–N(1)	95.2(2)
P(2)–Ru(1)–N(1)	172.6(2)	Cl(2)–Ru(2)–Cl(3)	87.93(9)
Cl(2)–Ru(2)–S(2)	172.01(9)	Cl(2)–Ru(2)–P(3)	90.67(10)
Cl(2)–Ru(2)–P(4)	96.13(10)	Cl(2)–Ru(2)–N(2)	82.5(2)
Cl(3)–Ru(2)–S(2)	92.09(8)	Cl(3)–Ru(2)–P(3)	178.39(9)
Cl(3)–Ru(2)–P(4)	91.68(9)	Cl(3)–Ru(2)–N(2)	87.3(2)
S(2)–Ru(2)–P(3)	89.18(9)	S(2)–Ru(2)–P(4)	91.86(9)
S(2)–Ru(2)–N(2)	89.5(2)	P(3)–Ru(2)–P(4)	89.27(10)
P(3)–Ru(2)–N(2)	91.7(2)	P(4)–Ru(2)–N(2)	178.3(2)

[a] See Figure 1 for the atom-labeling scheme. [b] Numbers in parentheses are estimated standard deviations for the last significant digit.

and angles are summarized in Table 3. Complex **5** preserves the two P(OMe)$_3$ in cis positions, the μ-N$_2$H$_4$ bridge, and the terminal chloride trans to the bridging sulfur atom of complex **1**. The mean Ru–S distance of 2.197 Å is typical for the Ru^{3+} dinuclear complexes.[1] The mean distances of Ru–P (2.269 Å),

10916   *J. Am. Chem. Soc., Vol. 121, No. 47, 1999*

Matsumoto et al.

Table 2. Comparison of Selected Bond Distances (Å) and Angles (deg) for **1** and **4**[a]

	1	**4**
bond distances		
Ru$-$Cl$_{terminal}$ (av)	2.442	2.410
Ru$-$Cl$_{bridging}$ (shortest)	2.477(2)	2.463(2)
Ru$-$S (av)	2.281	2.198
Ru$-$N (av)	2.171	2.193
Ru$-$P$_{trans\ to\ N}$ (av)	2.222	2.263
Ru$-$P$_{trans\ to\ Cl}$ (av)	2.217	2.231
S$-$S	2.002(3)	1.968(3)
N$-$N	1.442(1)	1.45(1)
bond angles		
Ru$-$S$-$S$-$Ru	16.1(2)	9.3(2)
Ru$-$N$-$N$-$Ru	56.5(7)	46.0(8)

[a] Numbers in parentheses are estimated standard deviations for the last significant digit.
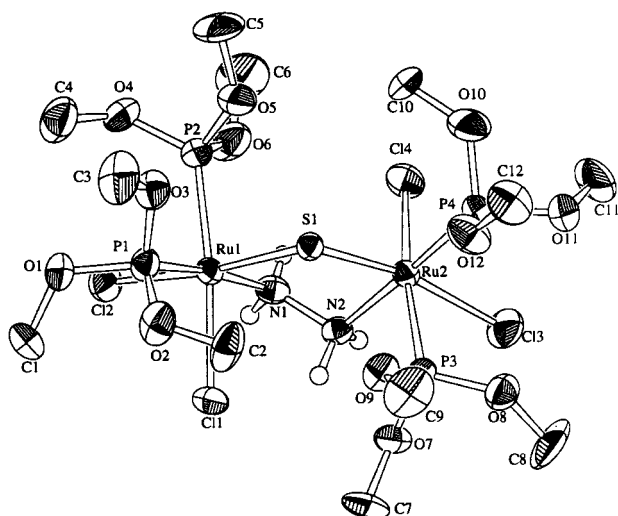
Figure 3. ORTEP diagram of {RuCl$_2$[P(OMe)$_3$]$_2$}$_2$(μ-S)(μ-N$_2$H$_4$) (**5**)·CH$_3$CN showing 50% probability thermal ellipsoids for all non-hydrogen atoms.

Ru$-$Cl$_{terminal}$ (2.448 Å), and Ru$-$N (2.169 Å) are all practically identical with those values found in complexes **1** and **4**. The μ-S^{2-} bridge in **5** must result from desulfurization of the μ-S$_2^{2-}$ bridge in **1**. It is noteworthy, however, that when the site symmetry of the common ligands at the two Ru centers of **1** and **5** are compared, the two site symmetries form enantiomers in **1** while they form a stereoisomer in **5** (Scheme 4). This must be the consequence of a conversion of the bridging chloride to the terminal chloride, and subsequent coordination of the fourth Cl atom.

Structural Characterization of {RuCl[P(OMe)$_3$]$_2$}$_2$(μ-S$_2$O$_5$)(μ-N$_2$H$_4$) (3). An ORTEP diagram of {RuCl[P(OMe)$_3$]$_2$}$_2$-(μ-S$_2$O$_5$)(μ-N$_2$H$_4$) (**3**), along with the atom-labeling scheme, is shown in Figure 4. Selected bond distances and angles are given in Table 4. Among the isolated products, only complex **3** has the Ru^{2+}Ru^{2+} oxidation state. The coordination geometry around the Ru atom is a distorted octahedron with the two P(OMe)$_3$ in cis positions, the terminal chloride, the μ-N$_2$H$_4$ bridge, and the μ-S$_2$O$_5^{2-}$-$O,S':O',S$ bridge. A close examination of the μ-S$_2$O$_5^{2-}$-$O,S':O',S$ bridge, which finds no precedence, shows that it consists of two SO$_2$ groups and the bridging oxygen atom sitting on a pseudo C_2 axis. Another S$_2$O$_5^{2-}$ moiety is structurally identified in [Fe(Me$_6$[14])-4,11-dieneN$_4$(S$_2$O$_5$)], where the S$_2$O$_5^{2-}$ moiety is composed of S(=O)O and S(=O)$_2$O groups, linked via S$-$S bond.[14] In complex **3**, the average S$-$O$_{\mu-oxo}$ distance of 1.69(1) Å corresponds to a single bond, and the

Table 3. Selected Bond Distances (Å) and Angles (deg) for **5**[a]

Bond Distances			
Ru(1)$-$Cl(1)	2.435(2)	Ru(1)$-$Cl(2)	2.456(2)
Ru(1)$-$S(1)	2.199(2)	Ru(1)$-$P(1)	2.254(2)
Ru(1)$-$P(2)	2.281(2)	Ru(1)$-$N(1)	2.169(6)
Ru(2)$-$Cl(3)	2.465(2)	Ru(2)$-$Cl(4)	2.436(2)
Ru(2)$-$S(1)	2.194(2)	Ru(2)$-$P(3)	2.283(2)
Ru(2)$-$P(4)	2.256(2)	Ru(2)$-$N(2)	2.169(6)
N(1)$-$N(2)	1.465(8)		

Bond Angles			
Cl(1)$-$Ru(1)$-$Cl(2)	88.24(6)	Cl(1)$-$Ru(1)$-$S(1)	99.46(6)
Cl(1)$-$Ru(1)$-$P(1)	89.46(7)	Cl(1)$-$Ru(1)$-$P(2)	170.32(7)
Cl(1)$-$Ru(1)$-$N(1)	84.5(2)	Cl(2)$-$Ru(1)$-$S(1)	168.50(7)
Cl(2)$-$Ru(1)$-$P(1)	95.79(7)	Cl(2)$-$Ru(1)$-$P(2)	82.49(7)
Cl(2)$-$Ru(1)$-$N(1)	85.1(2)	S(1)$-$Ru(1)$-$P(1)	92.83(7)
S(1)$-$Ru(1)$-$P(2)	89.31(7)	S(1)$-$Ru(1)$-$N(1)	87.2(2)
P(1)$-$Ru(1)$-$P(2)	94.22(8)	P(1)$-$Ru(1)$-$N(1)	173.8(2)
P(2)$-$Ru(1)$-$N(1)	92.0(2)	Cl(3)$-$Ru(2)$-$Cl(4)	86.22(7)
Cl(3)$-$Ru(2)$-$S(1)	168.61(7)	Cl(3)$-$Ru(2)$-$P(3)	82.32(7)
Cl(3)$-$Ru(2)$-$P(4)	96.79(7)	Cl(3)$-$Ru(2)$-$N(2)	84.3(2)
Cl(4)$-$Ru(2)$-$S(1)	101.17(7)	Cl(4)$-$Ru(2)$-$P(3)	168.35(7)
Cl(4)$-$Ru(2)$-$P(4)	93.51(7)	Cl(4)$-$Ru(2)$-$N(2)	84.4(2)
S(1)$-$Ru(2)$-$P(3)	89.86(7)	S(1)$-$Ru(2)$-$P(4)	91.44(7)
S(1)$-$Ru(2)$-$N(2)	87.8(2)	P(3)$-$Ru(2)$-$P(4)	89.92(7)
P(3)$-$Ru(2)$-$N(2)	92.4(2)	P(4)$-$Ru(2)$-$N(2)	177.5(2)

[a] See Figure 3 for the atom-labeling scheme.
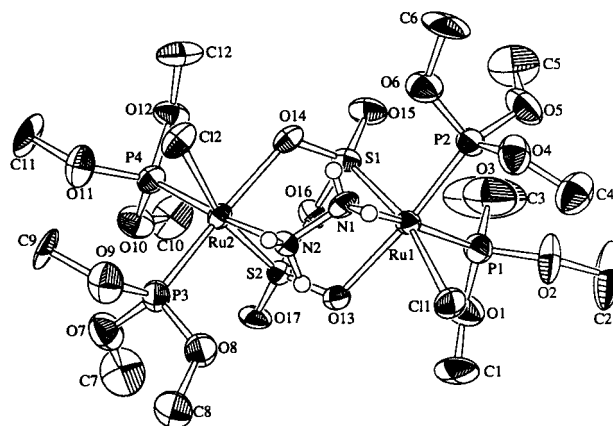
Figure 4. ORTEP diagram of {RuCl[P(OMe)$_3$]$_2$}$_2$(μ-S$_2$O$_5$)(μ-N$_2$H$_4$) (**3**) showing 50% probability thermal ellipsoids for all non-hydrogen atoms.

Scheme 4
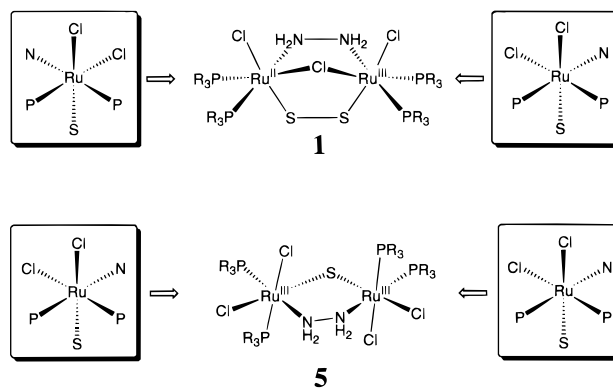
average S$-$O$_{terminal}$ distance (1.43 Å) and the average S$-$O$_{\eta-O}$ distance (1.50 Å) are within the range of double bond character. The S$-$O$_{\eta-O}$ distance is longer than the S$-$O$_{terminal}$ distance because the oxygen atom is coordinated to the metal. The average Ru$-$O distance of 2.23 Å is significantly longer than the sum of the covalent radii of Ru and O (2.08 Å).

(14) Reynolds, M. S.; Holm, R. H. *Inorg. Chim. Acta* **1989**, *155*, 113.

Table 4. Selected Bond Distances (Å) and Angles (deg) for **3**^{a}

Bond Distances			
Ru(1)−Cl(1)	2.418(4)	Ru(1)−S(1)	2.221(4)
Ru(1)−P(1)	2.248(4)	Ru(1)−P(2)	2.214(5)
Ru(1)−O(13)	2.26(1)	Ru(1)−N(1)	2.18(1)
Ru(2)−Cl(2)	2.434(4)	Ru(2)−S(2)	2.219(4)
Ru(2)−P(3)	2.211(5)	Ru(2)−P(4)	2.250(4)
Ru(2)−O(14)	2.20(1)	Ru(2)−N(2)	2.16 (1)
N(1)−N(2)	1.48(2)		
Bond Angles			
Cl(1)−Ru(1)−S(1)	165.2(2)	Cl(1)−Ru(1)−P(1)	93.4(2)
Cl(1)−Ru(1)−P(2)	97.4(2)	Cl(1)−Ru(1)−O(13)	86.0(3)
Cl(1)−Ru(1)−N(1)	81.6(3)	S(1)−Ru(1)−P(1)	95.6(2)
S(1)−Ru(1)−P(2)	94.0(2)	S(1)−Ru(1)−O(13)	82.0(3)
S(1)−Ru(1)−N(1)	89.1(4)	P(1)−Ru(1)−P(2)	92.3(2)
P(1)−Ru(1)−O(13)	92.1(3)	P(1)−Ru(1)−N(1)	175.0(3)
P(2)−Ru(1)−O(13)	174.3(3)	P(2)−Ru(1)−N(1)	88.9(4)
O(13)−Ru(1)−N(1)	87.1(5)	Cl(2)−Ru(2)−S(2)	166.1(2)
Cl(2)−Ru(2)−P(3)	95.1(2)	Cl(2)−Ru(2)−P(4)	92.2(1)
Cl(2)−Ru(2)−O(14)	85.1(3)	Cl(2)−Ru(2)−N(2)	84.3(4)
S(2)−Ru(2)−P(3)	96.3(2)	S(2)−Ru(2)−P(4)	94.8(1)
S(2)−Ru(2)−O(14)	82.9(3)	S(2)−Ru(2)−N(2)	88.1(4)
P(3)−Ru(2)−P(4)	94.7(2)	P(3)−Ru(2)−O(14)	175.7(3)
P(3)−Ru(2)−N(2)	88.1(3)	P(4)−Ru(2)−O(14)	89.6(3)
P(4)−Ru(2)−N(2)	175.7(4)	O(14)−Ru(2)−N(2)	87.6(4)

^{a} See Figure 5 for the atom-labeling scheme.
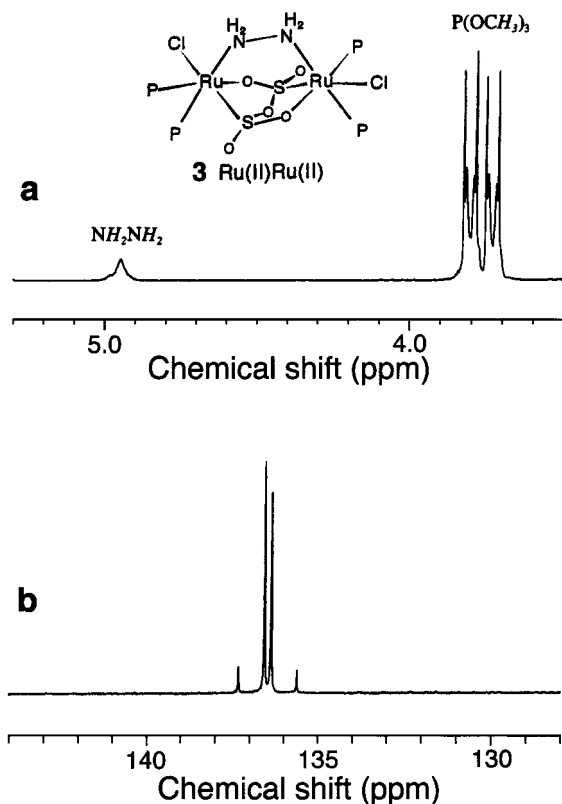
Figure 5. ^{1}H (top) and ^{31}P{^{1}H} (bottom) NMR spectra of **3** recorded in CD$_2$Cl$_2$ at room temperature.

Figure 6. ^{1}H (top) and ^{31}P{^{1}H} (bottom) NMR spectra of **4** recorded in CD$_3$CN at room temperature.
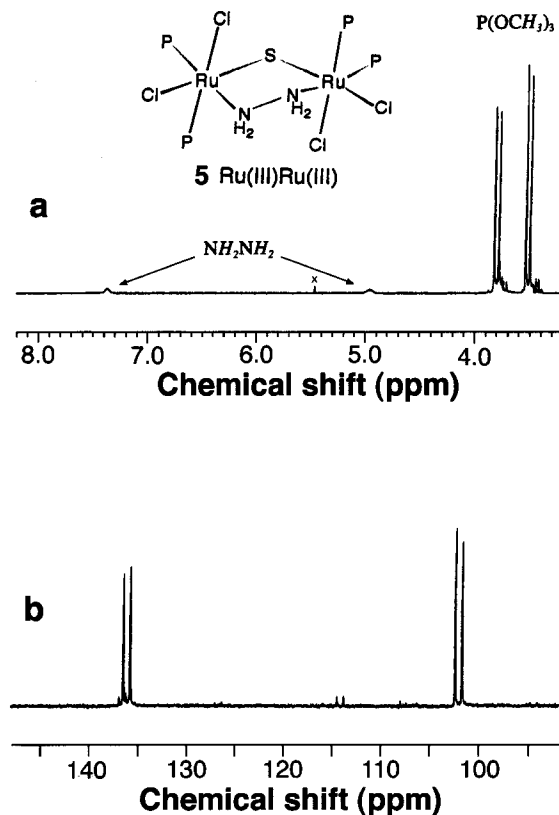
Figure 7. ^{1}H (top) and ^{31}P{^{1}H} (bottom) NMR spectra of **5** recorded in CD$_3$CN at room temperature.

NMR Spectral Assignments of 3, 4, and 5. The room temperature ^{1}H and ^{31}P{^{1}H} NMR spectra of **3**, **4**, and **5** are shown in Figures 5, 6, and 7, respectively, and the ^{1}H and ^{31}P chemical shifts are tabulated in Tables 5 and 6, respectively.

All the NMR spectra are recorded in CD$_3$CN except **3** in CD$_2$Cl$_2$.

In the ^{1}H NMR spectrum of **3**, a low-resolution broad peak at δ 4.94 is assigned to the two NH_2 protons, which split into two independent peaks at δ 5.03 and 4.82 at low temperature (−90 °C). The methoxy groups show a pair of doublets at δ

3.80 and 3.73. In the ^{31}P{^{1}H} NMR spectrum, a pair of doublets (δ 137.0 and 136.0, J_{PP} = 83.7 Hz) of the two phosphorus atoms are separated by only 1.0 ppm, suggesting the two P(OR)$_3$ ligands are stereochemically alike.

**Table 5.** ^{1}H NMR Data for Complexes **3**, **4**, and **5**[a,b]

compound	$\delta(N_2H_4)$	$\delta(P(OCH_3)_3)$
{RuCl[P(OMe)$_3$]$_2$}$_2$- (μ-S$_2$O$_5$)(μ-N$_2$H$_4$) (**3**)	4.94 (s (br), 4H)	3.80 (d, 10.6, 9H) 3.73 (d, 10.6, 9H)
{RuCl[P(OMe)$_3$]$_2$}$_2$- (μ-S$_2$)(μ-Cl)(μ-N$_2$H$_4$)$^+$ (**4**)	5.22 (s, 2H) 5.00 (s, 2H)	3.90 (d, 10.3, 9H) 3.67 (d, 10.3, 9H)
{RuCl$_2$[P(OMe)$_3$]$_2$}$_2$- (μ-S)(μ-N$_2$H$_4$) (**5**)	7.38 (s, 2H) 4.96 (s, 2H)	3.81 (d, 9.5, 9H) 3.52 (d, 9.5, 9H)

^{a} NMR spectra of **4** and **5** are recorded in CD$_3$CN, and **3** in CD$_2$Cl$_2$. ^{b} Chemical shifts are reported in ppm and J_{HP} in Hz (in parentheses).

Table 6. ^{31}P{^{1}H} NMR Data for Complexes **3**, **4**, and **5**[a,b]

compound	$\delta(P(OCH_3)_3)$
{RuCl[P(OMe)$_3$]$_2$}$_2$(μ-S$_2$O$_5$)- (μ-N$_2$H$_4$) (**3**)	137.0 (d, 83.7), 136.0 (d, 83.7)
{RuCl[P(OMe)$_3$]$_2$}$_2$(μ-S$_2$)(μ-Cl)- (μ-N$_2$H$_4$)$^+$(**4**)	126.0 (d, 81.6), 115.7 (d, 81.6)
{RuCl$_2$[P(OMe)$_3$]$_2$}$_2$(μ-S)- (μ-N$_2$H$_4$) (**5**)	136.0 (d, 79.0), 102.0 (d, 79.0)

^{a} NMR spectra are recorded in CD$_3$CN. ^{b} Chemical shifts are reported in ppm and J_{PP} in Hz (in parentheses).
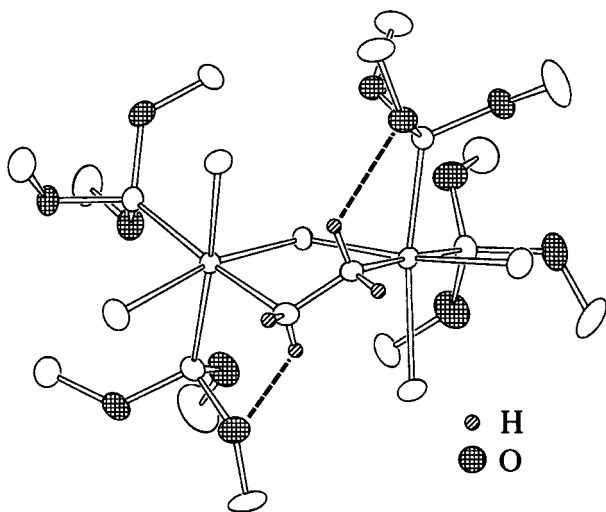

Figure 8. Intramolecular hydrogen bond diagram of **5**.

In the ^{1}H NMR spectrum of complex **4**, the two N*H$_2$* protons appear at δ 5.22 and 5.00. The methoxy group exhibits a pair of doublets at δ 3.90 and 3.67 due to the two different P(OMe)$_3$ environments. The ^{31}P{^{1}H} NMR chemical shifts of the cis-coordinated P(OMe)$_3$ exhibit two doublets at δ 126.0 (trans to N) and 115.7 (trans to Cl) with J_{PP} = 81.6 Hz.

The ^{1}H NMR spectrum of **5** shows the largest chemical shift difference between the two N*H$_2$* protons due to a significant downfield shift of one of the protons caused by an asymmetric intramolecular hydrogen bond (Figure 8). Two doublets of the methoxy protons appear at δ 3.81 and 3.52. In the ^{31}P{^{1}H} NMR spectrum, the two phosphorus nuclei resonate at δ 136.0 and 102.0 (J_{PP} = 79.0 Hz), assigned to the phosphorus trans to N and trans to Cl, respectively.

NMR Spectral Studies of the Oxidation Reaction. An CD$_3$-CN solution of **1** is sealed in an NMR tube under oxygen and its room temperature aging is monitored by ^{1}H NMR spectroscopy (Figure 9).

Figure 9a shows the spectrum observed 0.2 h after oxygen intake. A broad resonance at ca. δ 5.1 is an averaged resonance of **1** and a diamagnetic species. The low-resolution signal at δ 3.8 is considered to consist of a number of transient diamagnetic species. After 1.5 h, the averaged resonance becomes increas-
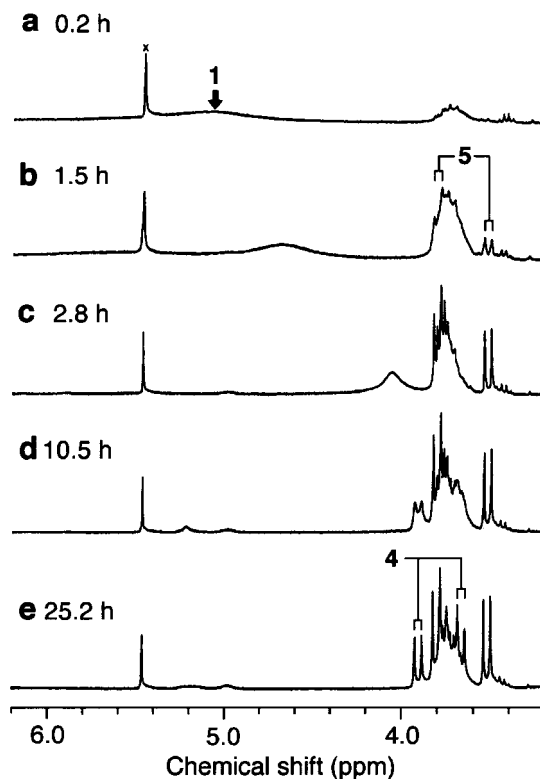
Figure 9. ^{1}H NMR spectra of the aging of **1** under O$_2$ measured in CD$_3$CN.

ingly noticeable and shifts upfield (δ 4.6), indicative of exhaustive oxidation of **1** to the diamagnetic species (Figure 9b). Among the diamagnetic species (δ 3.4−3.9), complex **5** (doublets at δ 3.81 and 3.52) already can be recognized at this stage. After 2.8 h, the averaged resonance shifts to δ 4.1, and complex **5** becomes prominent (Figure 9c). After 10.5 h, the averaged resonance seems to convert to the two doublets (δ 3.9 and 3.7). Those doublets coincide with those of complex **4** (=**1**$^+$HSO$_4^-$) (Figure 9d), and as is surmised at the initial stage of the oxidation, **1** is oxidized to generate **1**$^+$O$_2^-$, the charge-transfer product consisting of the one-electron oxidized Ru dimer and a one-electron reduced oxygen, and as the oxidation progresses, **1**$^+$O$_2^-$ converts to spectroscopically indistinguishable **4**. After 25.2 h complex **1** is exhausted, and the spectrum consists of sharp doublets of complex **4** and **5**.

The oxidation reaction is also observed by ^{31}P{^{1}H} NMR spectroscopy. Figure 10 shows the P(OMe)$_3$ region of the spectra.[15] Although complex **3** is hardly soluble, it is barely recognized at δ 136.0 and 102.0 (Figure 10a), along with **5**. The next two spectra clearly show that equilibrium is being less and less favorable to **1** (Figures 10b and 10c). The oxidation reaction has completed in 22.2 h, and the spectrum consists predominantly of **2**, **4**, and **5** (Figure 10d).

To retard the reaction and investigate the initial stage of the oxidation, ^{31}P{^{1}H} NMR spectra are observed at −35 °C (Figures 11). The reaction slows down significantly at this temperature, and **1** and **1**$^+$O$_2^-$ are still equilibrating even after 11 h as is evident from the broad resonances at δ 126 and 116 (Figure 11a). A cluster of signals (δ 127−154) must stem from oxo complexes of various isomeric forms. When the solution is briefly warmed to room temperature, complex **5** appears at the expense of **1**$^+$O$_2^-$ (Figure 11b), presumably because a part

(15) Empirically we are aware of the ^{31}P NMR chemical shifts in the P(OMe)$_3$ ligand that falls at around 123 ppm for a Ru^{3+}Ru^{3+} complex and >135 ppm for a Ru^{2+}Ru^{2+} complex. See for example, ref 1.

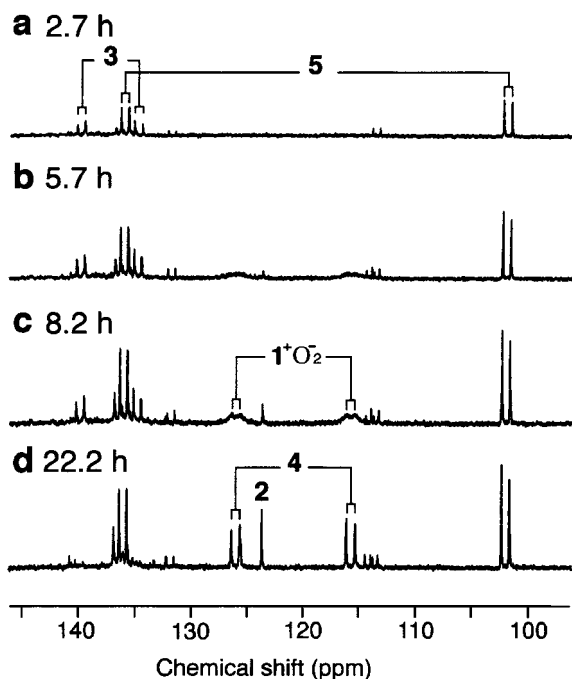**Figure 10.** $^{31}P\{^1H\}$ NMR spectra of the aging of **1** under O$_2$ measured in CD$_3$CN.

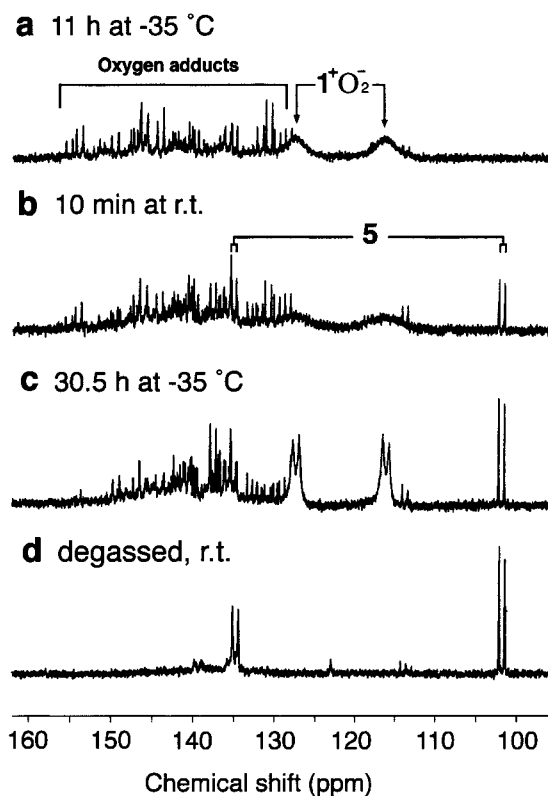**Figure 11.** $^{31}P\{^1H\}$ NMR spectra of the low-temperature (-35 °C) aging of **1** under O$_2$ measured in CD$_3$CN.

of **1**$^+$O$_2^-$ reverts to **1** and the rest yields the products. After 30.5 h, still **1**$^+$O$_2^-$ must be the major contributor to the two doublets (δ 126 and 116) (Figure 11c), because freeze−pump−thaw erased the doublets (Figure 11d), indicating that **1**$^+$O$_2^-$ accumulates when O$_2^-$ is abundant, i.e., **1** + O$_2$ ↔ **1**$^+$ + O$_2^-$ ↔ **1**$^+$O$_2^-$.

The Oxygen Activation Mechanism. It is known that a certain ruthenium complex has the ability to activate oxygen in an olefin epoxidation reaction.[16] However, dioxygen is usually

Scheme 5
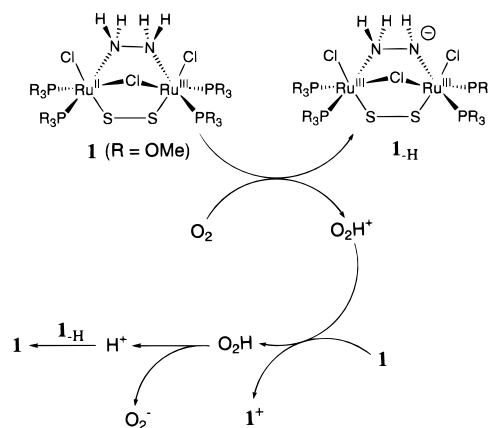
kinetically inert and the direct transfer of an electron from the metal to oxygen occurs only when the reduction potential of the metal complex is more negative than that of O$_2$ (eq 1).[17]

$$L_xM^n + O_2 \leftrightarrow L_xM^{n+1} + O_2^- \tag{1}$$
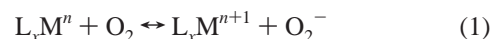
Komatsuzaki and co-workers recently reported the oxygen activation in toluene by the Mn^{2+} thiolate complex, yielding the Mn^{3+} bis μ-O complex.[18] They confirmed that the Mn carboxylate complex is ineffective under the same condition because carboxylate is not as an good electron donor as thiolate, which is capable of driving the reduction potential of the Mn complex negative enough for the oxygen activation. Previously, we estimated $E°(\mathbf{1}^{0/+1}:Ru^{2+}Ru^{3+}/Ru^{3+}Ru^{3+})$ to fall in the vicinity of -0.29 V vs NHE in CH$_2$Cl$_2$,[19] which precludes the possibility of direct oxygen reduction ($E°(O_2/O_2^-) = -0.60$ V vs NHE in DMF).[20] However, if protonation of O$_2$ precedes, the reduction potential of O$_2$H$^+$ becomes considerably more positive (0.12 V vs NHE in DMF) than that of O$_2$, and enables **1** to **1**$^+$ oxidation. Considering our observation that the oxidation reaction is characteristic to the dinuclear Ru complexes with the μ-N$_2$H$_4$ bridge and the hydrazine-free complexes are stable in air,[21] the bridging hydrazine must protonate dioxygen to O$_2$H$^+$ (Scheme 5). The hydroperoxyl radical, O$_2$H, is expected to be generated as a result of the oxidation reaction. The hydroperoxy radical is unstable and produces O$_2^-$ and H$^+$, which may be used in protonation of **1**$_{-H}$ to **1**.

A widely used O$_2^-$ generator, KO$_2$/18-crown-6,[22] was reacted with a CH$_3$CN solution of **4** to verify O$_2^-$ participation in the oxidation. In about 4 h after the addition of KO$_2$/18-crown-6, the solution turned from green to blue, and an unknown precipitate was formed in the solution. Complex **5** is identified in the $^{31}P\{^1H\}$ NMR spectrum of the reaction solution, presumably because **4** reverts to **1**$^+$O$_2^-$ in the presence of excess O$_2^-$, and then converts to **5**. When complex **1** was reacted with KO$_2$/18-crown-6, however, the solution turned yellow and the

(16) Stultz, L. K.; Binstead, R. A.; Reynolds, M. S.; Meyer, T. J. *J. Am. Chem. Soc.* **1995**, *117*, 2520.

(17) Cotton, F. A.; Wilkinson, G. *Advanced Inorganic Chemistry*, 5th ed.: Wiley: New York, 1988; pp 468−471 and references therein.

(18) Komatsuzaki, H.; Nagasu, Y.; Suzuki, K.; Shibasaki, T.; Satoh, M.; Ebina, F.; Hikichi, S.; Akita, M.; Moro-oka, Y *J. Chem. Soc., Dalton Trans.* **1998**, 511.

(19) The value in ref 1h (-0.09 V vs Ag/AgCl) is converted by subtracting -0.197 V. See Bard and Faulkner (Bard, A. J.; Faulkner, L. R. *Electrochemical Methods*: Wiley: New York, 1980) for the conversion table.

(20) Sawyer, D. T.; Valentine, J. S. *Acc. Chem. Res.* **1981**, *14*, 393.

(21) Koyama, T. M.S. Thesis, Waseda University, Tokyo, Japan, 1997.

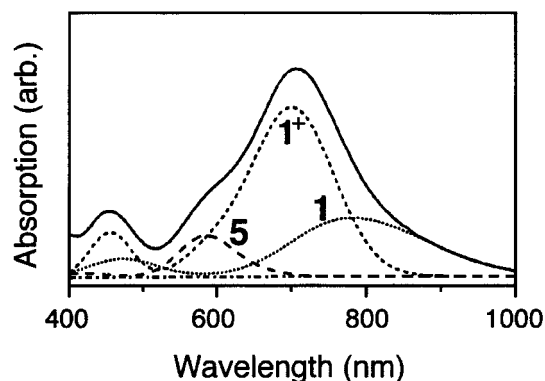(22) Espenson, J. H. *Inorg. Chem.* **1983**, *22*, 847.

Figure 12. UV−vis spectrum of the reaction solution (solid line) recorded at $t = 5$ h in CH_3CN and the deconvoluted curves of **1** (···), **1$^+$** (- - -), and **5** (- − -). Here, **1$^+$** consists of **1$^+$O$_2^-$** and **4**.
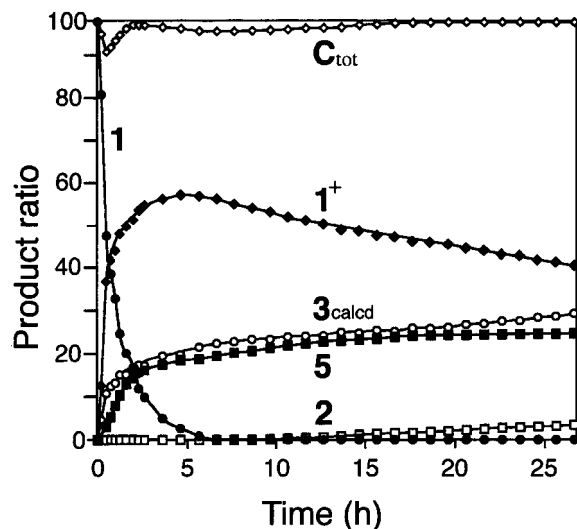

Figure 13. Plot of the time course of the concentrations of **1**, **1$^+$**, **2**, and **5** estimated from the UV−vis spectra and the calculated curve for **3**. The percent ratio of each products are normalized to [**1**] = 100 at $t = 0$ h.

^{31}P{^{1}H} NMR spectrum exhibited many unidentifiable peaks, indicative of the decomposition.

UV−Vis Spectral Analysis of the Product Balance and the Reaction Process. Information supporting the oxidation reaction mechanism was obtained by observing the time course of the reactant and products using UV−vis spectroscopy. The absorption spectra of the reaction solution were recorded in CH_3-CN every 10−50 min over 27 h, and a 520−1000 nm region of each spectrum was deconvoluted to obtain the absorption spectrum of each product. A representative UV−vis spectrum of the reaction solution along with the results of the deconvolution are shown in Figure 12.[23] The concentration of each product is calculated using the extinction coefficient of each compound, **1**, **1$^+$** (= **1$^+$O$_2^-$** + **4**), **2**, and **5** (negligible in Figure 12). The concentrations of **1**, **1$^+$**, **2**, and **5** are plotted as a function of time in Figure 13. Although **3** is precluded from direct observation due to its poor solubility, we circumvented the problem by applying the following assumptions: (a) **3** has

one less Cl atom than **1**, and the lost Cl atoms are passed on to **2** and **5**, and (b) **5** has one less S atom than **1**, and the lost S atom is consumed for the formation of HSO_4^- in **4**. From these assumptions, the following relations (eqs 2 and 3) can be readily derived.

$$[\mathbf{3}] = [\mathbf{2}] + [\mathbf{5}] \qquad (2)$$

$$[\mathbf{4}] = [\mathbf{5}] \qquad (3)$$

The sum of the concentrations of the products ($[\mathbf{C}_{tot}]$) is defined by eq 4 and the result is plotted in Figure 13.

$$[\mathbf{C}_{tot}] = [\mathbf{1}^+] + [\mathbf{2}] + [\mathbf{3}] + [\mathbf{5}] \cong [\mathbf{1}^+] + [\mathbf{2}] + ([\mathbf{2}] + [\mathbf{5}]) + [\mathbf{5}] \quad (4)$$

Except for the initial 1.5 h when **1** and **1$^+$** dominate the spectrum and the baseline is unstable, $[\mathbf{C}_{tot}]$ deviates little from unity throughout the reaction, indicating **2**−**5** are the dominant products. Therefore, the oxidation reaction can be balanced as follows:

$$14 \times \mathbf{1} + 4.5\ O_2 = \mathbf{2} + 5 \times \mathbf{3} + 4 \times \mathbf{4} + 4 \times \mathbf{5} \quad (5)$$
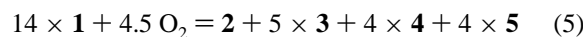
Also, the concentration of complex **3** can be defined by eq 6, and the result is plotted in Figure 13.

$$[\mathbf{3}_{calcd}] = 100 - ([\mathbf{1}^+] + [\mathbf{2}] + [\mathbf{5}]) \qquad (6)$$

In the first hour, $[\mathbf{1}^+]$ accumulates rapidly at the expense of $[\mathbf{1}]$, apparently indicating that **1$^+$** is the prime product. Then accumulation of $[\mathbf{3}_{calcd}]$ and $[\mathbf{5}]$ follows in this order. The curve of $[\mathbf{3}_{calcd}]$ eases off after ca. 10% is reached, while the curve of $[\mathbf{5}]$ continues to rise. However, $[\mathbf{5}]$ never exceeds $[\mathbf{3}_{calcd}]$, and the production of **5** also slows down when it reaches ca. 10%. Hereafter, $[\mathbf{5}]$ and $[\mathbf{3}]$ draw almost identical curves, supporting assumption (a).

^{18}O$_2$/^{16}O$_2$ Isotope Labeling Studies. To ascertain participation of atmospheric oxygen in HSO_4^- and $S_2O_5^{2-}$ moieties of complexes **3** and **4**, respectively, the oxidation reaction was conducted under a mixture of ^{18}O$_2$/^{16}O$_2$ (70/30 vol %) oxygen isotopes, and each product was isolated as a crystal, which were subjected to IR spectroscopic analysis. Figure 14 shows, from top to bottom, the S=O stretching bands of **1**, **3**, **3** prepared in ^{18}O$_2$/^{16}O$_2$, **4**, and **4** prepared in ^{18}O$_2$/^{16}O$_2$. The band assignments are summarized in Table 7.[24,25] The S=O stretching bands of **3**, $\nu(S-O_{S-O-S})/\nu(S=O_{S-O-Ru})/\nu(S=O_{terminal})$ at 987/1236/1251 cm^{-1}, are overlapped by ^{18}O labeled analogues at 960/1192/1213 cm^{-1} in labeled **3**. The S=^{16}O stretching band of **4** (1161 cm^{-1}) is weakened in labeled **4**, replaced by $\nu(S=^{18}O)$ at 1130 cm^{-1}. The above observation confirms that external oxygen is used in the oxidation reaction.

Darensbourg and co-workers have extensively investigated the oxidation mechanisms of the Ni−sulfur complex to the Ni bis-sulfinate complex, where intramolecular O_2 coordination and subsequent O−O bond scission are proposed as the principle pathway (Scheme 6).[9a,26] They showed that the sulfide oxidation proceeds with 85% intramolecular and 15% intermolecular O−O

(23) Curve fitting was performed using the following equation, $F(x) = \lambda(\mathbf{1})\{\exp[-((x - 585)/51.5)^2] + 0.115\ \exp[-((x - 654)/50.9)^2]\} + \lambda(\mathbf{1}^+)\{\exp[-((x - 778)/116)^2] + 0.217\ \exp[-((x - 923.9)/108.4)^2]\} + \lambda(\mathbf{2})\ \exp[-((x - 733)/89.04)^2] + \lambda(\mathbf{5})\{\exp[-((x - 700)/81.4)^2] + 0.117\ \exp[-((x - 586.4)/49.9)^2]\} + W_{bkgd}$, where W_{bkgd} is the background absorbance, and $\lambda(\mathbf{n})$ (nm) is the visible absorption maximum of complex **n**. The molar extinction coefficients (ϵ, M^{-1}cm^{-1}) used are 2666 for **1**, 7073 for **1$^+$**, 6779 for **2**, and 7457 for **5**.

(24) (a) Miller, C. A.; Janik, T. S.; Churchill, M. R.; Atwood, J. D. *Inorg. Chem.* **1996**, *35*, 3683. (b) Randall, S. L.; Thompson, J. S.; Buttrey, L. A.; Ziller, J. W.; Churchill, M. R.; Atwood, J. D. *Organometallics* **1991**, *10*, 683. (c) Valentine, J.; Valentine, D., Jr.; Collman, J. P. *Inorg. Chem.* **1971**, *10*, 219. (d) Horn, R. W.; Weissberger, E.; Collman, J. P. *Inorg. Chem.* **1970**, *9*, 2367.

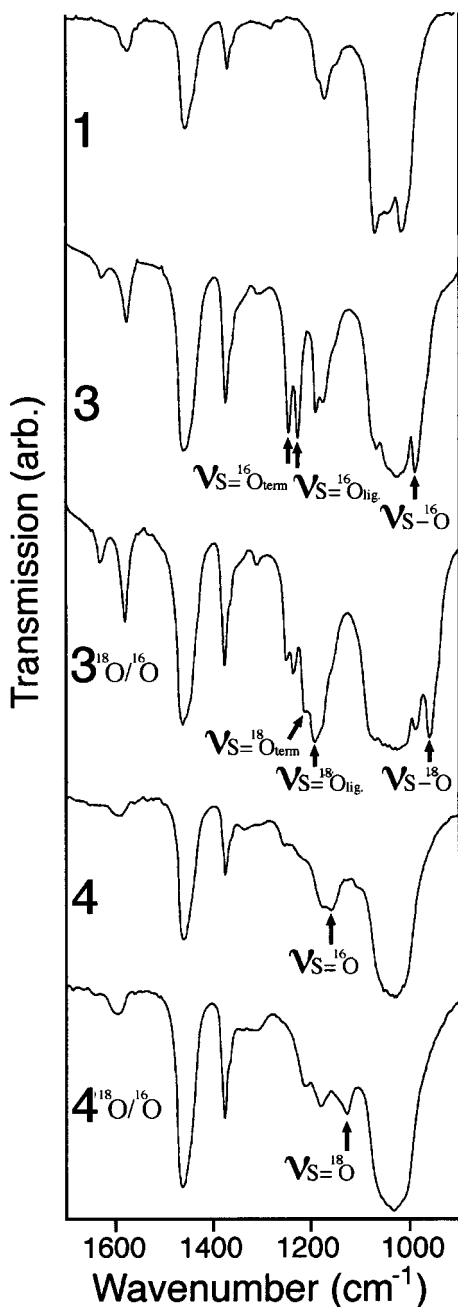(25) Mingos, D. M. P. *Transition Met. Chem.* **1978**, *3*, 1.

Oxidation of the Sulfide Ligands to SO₄²⁻

J. Am. Chem. Soc., Vol. 121, No. 47, 1999 10921

Scheme 6

Scheme 7

Figure 14. IR absorption spectra of the S=O stretching region (1700–900 cm⁻¹) of, from top to bottom, **1**, **3**, **3** prepared in ¹⁸O₂/¹⁶O₂, **4**, and **4** prepared in ¹⁸O₂/¹⁶O₂. The samples were prepared by grinding in mineral oil.

Table 7. The Isotopic Shift in IR Absorption Bands in Complexes **3** and **4**

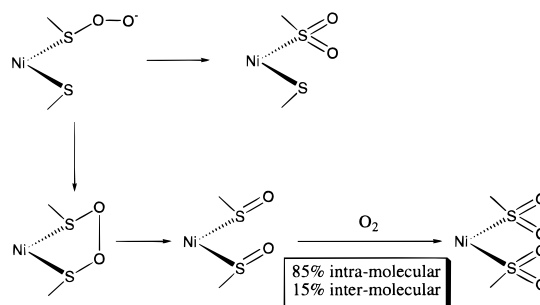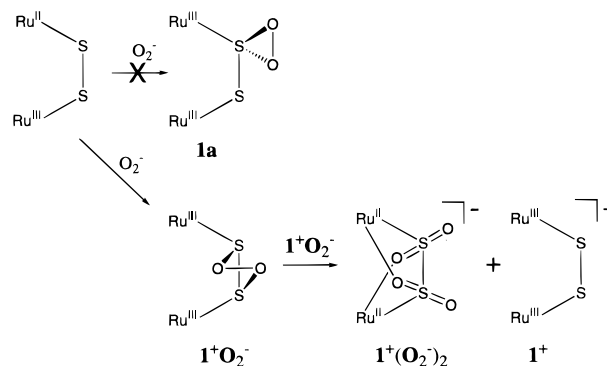| compd	¹⁶O (cm⁻¹)	¹⁸O (cm⁻¹)	assign
3	1251 (s, sh)	1213 (s, sh)	ν(S=O)[a]
	1236 (s, sh)	1192 (s, sh)	ν(S=O)[b]
	982 (s, sh)	960 (s, sh)	ν(S–O)
4	1161 (m, br)	1130 (m, br)	ν(S=O)

[a] Terminal S=O. [b] Ru ligating S=O.

bond scission. In case of the oxidation of complex **1**, however, due to the significantly shorter S–S distance compared to the Ni bis-sulfinate, the initial O_2^- coordination is expected to result

almost exclusively in the formation of η^2,μ-O₂-*S,S* in lieu of η^2-O₂ (**1a**) (Scheme 7),[27] and $\mathbf{1}^+O_2^-$ converts via disproportionation to form $\mathbf{1}^+$ and the dithionite complex, $\mathbf{1}^+(O_2^-)_2$. Such dithionite complex is already known in other system.[28d28] In the disproportionation process, however, it is unknown whether the O–O bond cleavage[28] occurs prior to the O_2^- transfer or not.

The Oxidation Reaction Mechanism. On the basis of the above observations, the most plausible reaction pathways are schematized in Scheme 8. The initial stage includes oxygen activation and disproportionation of $\mathbf{1}^+O_2^-$, forming the dithionite complex, $\mathbf{1}^+(O_2^-)_2$,[28d] and $\mathbf{1}^+$. The dithionite complex undergoes coordination rearrangement of a dithionite bridge and Cl⁻ dissociation to prepare a neutral intermediate **I** (pathway **A**), which reacts further with O_2^- to generate the $S_2O_5^{2-}$ moiety in complex **3** by the intermolecular O_2^- coordination and homolytic O–O bond cleavage (Scheme 9).[9a,25,29]The resulting **3**⁻ may be utilized in further oxygen activation.

The liberated Cl⁻ may induce the SO_4^{2-} dissociation from the anionic dithionite complex, leading to the formation of complex **5** (pathways **B** and **C**). The liberated SO_4^{2-} must become the source of the HSO_4^- counteranion in **4** (pathway **D**). Complex **4** is, however, unstable when $[O_2^-]$ exceeds $[HSO_4^-]$ as demonstrated in the reaction of **4** with KO₂/18-crown-6, and when O_2^- is abundant **4** will revert to $\mathbf{1}^+O_2^-$ (pathway **E**) (eq 7).

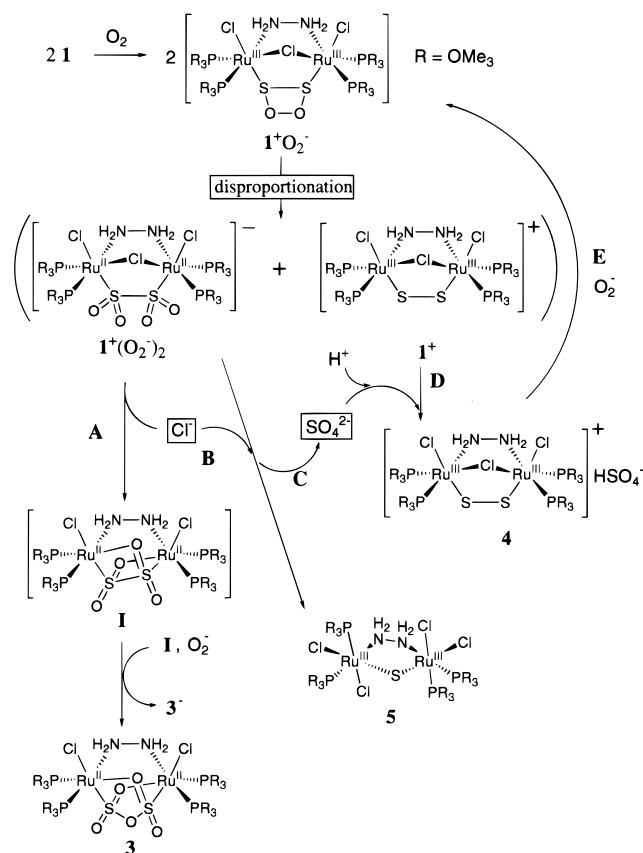$$\mathbf{4} \xrightarrow{O_2^-} \mathbf{1}^+O_2^- + HSO_4^- \tag{7}$$

This mechanism explains the reason complex **4** is not observed while complex **5** is present in Figure 11d.

(27) Duty, R. C.; Sahni, R.; Roark, R. *Phosphorus, Sulfur, and Silicon* **1996**, *116*, 9.

(28) Caradonna, J. P. *Encyclopedia of Inorganic Chemistry*; Wiley: New York, 1994; Vol. 6, p 2866.

(29) (a) Angoletta, M.; Bellon, P. L.; Manassero, M.; Sansoni, M. *J. Organomet. Chem.* **1974**, *81*, C40. (b) Kim, Y. H.; Lim, S. C.; Kim, K. S. *Pure Appl. Chem.* **1993**, *65*, 661.

(26) (a) Grapperhaus, C. A.; Darensbourg, M. Y. *Acc. Chem. Res.* **1998**, *31*, 451. (b) Buonomo, R. M.; Font, I.; Maguire, M. J.; Reibenspies, J. H.; Tuntulani, T.; Darensbourg, M. Y. *J. Am. Chem. Soc.* **1995**, *117*, 963.

Scheme 8

Scheme 9

Table 8. Crystal Data for **3**, **4**, and **5**

compd	3	4	5
formula	$C_{12}H_{40}N_2O_{12}$- $P_4S_2Cl_2Ru_2$	$C_{14}H_{41}N_3O_{16}$- $P_4S_3Cl_3Ru_2$	$C_{14}H_{43}N_3O_{12}$- $P_4SCl_4Ru_2$
fw	865.52	1036.06	945.41
cryst syst	monoclinic	monoclinic	monoclinic
space group	$P2_1/c$ (No. 14)	$P2_1/n$ (No. 14)	$P2_1/c$ (No. 14)
a, Å	15.862(5)	13.537(4)	9.863(5)
b, Å	12.551(6)	17.250(5)	14.785(4)
c, Å	17.541(5)	16.555(3)	24.622(3)
α, deg	90	90	90
β, deg	98.10(2)	101.91(2)	95.03(2)
γ, deg	90	90	90
V, Å^3	3457(2)	3782(1)	3576(1)
Z	4	4	4
d_{calcd}, g cm^{-3}	1.663	1.819	1.756
abs coeff (μ), cm^{-1}	13.80	14.08	14.31
radiation (λ), Å	Mo Kα 0.71069	Mo Kα 0.71069	Mo Kα 0.71069
R^a	0.056	0.045	0.037
$R_w{}^b$	0.071	0.049	0.038
GOF^c	1.08	1.39	3.70
T (deg)	20.0	20.0	20.0

^{a} $R = \sum(|F_o| - |F_c|)/\sum|F_o|$. ^{b} $R_w = [\sum w(|F_o| - |F_c|)^2/\sum w|F_o|^2]^{1/2}$; $w = 1/\sigma(F_o)^2$. ^{c} GOF $= [\sum w(|F_o| - |F_c|)^2/\sum(N_{reflcns} - N_{params})]^{1/2}$.

distilled and degassed prior to use. Solution NMR spectra were obtained on a JEOL HNM-EX270 spectrometer using either CD$_3$CN or CD$_2$-Cl$_2$. ^{31}P{^{1}H} NMR chemical shifts were recorded in reference to P(OMe)$_3$/(CD$_3$)$_2$CO external reference (140 ppm). UV–vis spectra were recorded on a Shimadzu UV-3101PC using a quartz cuvette with 1.0 cm optical path. Infrared (IR) spectra of the samples either pressed in KBr pellets or ground with mineral oil are obtained at a resolution of 4 cm^{-1} between 4000 and 400 cm^{-1} on a Hitachi I-3000 spectrometer either with a solution cell equipped with KBr windows or with KBr pellets. Negative FAB mass spectra were obtained using a nitrobenzyl alcohol matrix. The X-ray photoelectron spectra were recorded on a Perkin-Elmer Model 5600 spectrometer as described elsewhere.[1d] {RuCl[P(OMe)$_3$]$_2$}$_2$(μ-S$_2$)(μ-Cl)(μ-N$_2$H$_4$) (**1**) is prepared as previously described.[1h]

X-ray Crystallography. Crystals were covered with epoxy-resin and adhered to a glass tip and mounted on a goniometer of Rigaku AFC-7R four-circle automated diffractometer. Graphite-monochromated Mo Kα radiation (0.71069 Å) was employed. Data collection and cell determinations were performed in a manner previously described, using the θ–2θ scan technique.[1d] The Lorentz–polarization and absorption corrections were made to the collected data.[31] Pertinent details are given in Table 8. The structures were solved by a direct method, and the model was refined by using full-matrix least-squares techniques. In complex **4**, no solvent molecule was found despite an elemental analysis revealing the existence of 0.3 molecule of CH$_3$CN per complex molecule. Complex **5** crystallizes with and without a solvent molecule in the lattice. The monosolvate platelike crystals and the nonsolvate needlelike crystals are manually separated. The hydrogen atom coordinates were refined but their isotropic B's were held fixed. All non-hydrogen atoms were refined anisotropically. Pertinent crystallographic data are summarized in Table 8.

Synthesis of {RuCl[P(OMe)$_3$]$_2$}$_2$(μ-S$_2$O$_5$)(μ-N$_2$H$_4$) (3). A reddish-brown acetonitrile solution (10 mL) of {RuCl[P(OMe)$_3$]$_2$}$_2$(μ-S$_2$)(μ-Cl)(μ-N$_2$H$_4$) (**1**) (0.10 g, 0.11 mmol) was prepared in a 100 mL Schlenk flask under nitrogen atmosphere at room temperature. After slightly negative pressure was applied to the manifold and the flask, dry oxygen was introduced. Following the isolation of the flask, the solution was left undisturbed at room temperature for 25 h until it turns blue. The resulting colorless crystals of **3** were isolated and rinsed with 5 mL of diethyl ether. Yield: 33.3 mg, 32%. ^{1}H NMR (CD$_2$Cl$_2$): δ 4.94 [4H, s (br), NH_2NH_2], 3.80 [9H, d, J_{HP} = 10.6 Hz, P(OCH_3)$_3$], 3.73 [9H, d, J_{HP} = 10.6 Hz P(OCH_3)$_3$]. ^{31}P{^{1}H} NMR (CD$_2$Cl$_2$): 137.0 [d, J_{PP} = 83.7 Hz, P(OCH$_3$)$_3$], 136.0 [d, J_{PP} = 83.7 Hz, P(OCH$_3$)$_3$]. Anal. Calcd for $C_{12}H_{40}N_2O_{17}Cl_2S_2P_4Ru_2$: C, 15.24; H, 4.26; N, 2.96, Found: C, 15.09; H, 3.99; N, 2.98.

Conclusion

A room temperature reaction of complex **1** with oxygen yielded as many as three isolable products, and their structural characterization helped to understand the oxidation mechanism. Although details of the reaction mechanisms are still left unknown, coordination flexibility and activity of the SO$_n$ moiety on the Ru atom is considered to play an important role in the oxidation reaction.[30] We have shown that the oxidation state of the sulfur changes as the oxidation reaction proceeds from −1 in complex **1** to +6 in complex **3**. Considering the fact that certain bacterias produce SO$_4{}^-$ from sulfide at ambient temperature, the above oxidation reaction is highly interesting as the first example of an ultimate oxidation of S$^-$ to SO$_4{}^{2-}$ in a nonbiological system. We are particularly interested in development of the transition metal catalyzed sulfuric acid synthesis. The current system cannot function as a catalyst because complex **1** serves as the oxygen activator and the reactor, and is exhaustively consumed in the reaction. We are actively engaged in separation of those two functions to achieve a room temperature catalytic production of SO$_4{}^{2-}$.

Experimental Section

General Methods. All synthetic procedures were performed under purified nitrogen using standard Schlenk techniques or in an nitrogen atmosphere glovebox unless otherwise mentioned. Solvents were

(30) Kubas, G. J. *Acc. Chem. Res.* **1994**, *27*, 183.
(31) Walker, N.; Stuart, D. *Acta Crystallogr., Sect. A* **1983**, *A39*, 158.

Synthesis of [{RuCl[P(OMe)₃]₂}₂(μ-S₂)(μ-Cl)(μ-N₂H₄)]⁺HSO₄⁻ (4) and {RuCl₂[P(OMe)₃]₂}₂(μ-N₂H₄) (5). The resulting blue solution was evaporated to ca. 5 mL, layered with diethyl ether (20 mL), and left at room temperature for 24 h to obtain green crystals of **4**. Yield: 23.9 mg, 21%. ^{1}H NMR (CD₃CN): δ 5.22 [2H, s (br), N(H)HN(H)H], 5.00 [2H, s (br), N(H)HN(H)H], 3.90 [9H, d, J_{HP} = 10.3 Hz, P(OCH_3)₃], 3.67 [9H, d, J_{HP} = 10.3 Hz, P(OCH_3)₃]. ^{31}P{^{1}H} NMR (CD₃CN): 126.0 [d, J_{PP} = 81.6 Hz, P(OCH₃)₃], 115.7 [d, J_{PP} = 81.6 Hz, P(OCH₃)₃]. Anal. Calcd for C₁₂.₆H₄₁.₉N₂.₃O₁₆Cl₃S₃P₄Ru₂:[32] C, 14.99; H, 4.08; N, 3.19, Found: C, 14.81; H, 4.26; N, 2.97.

The blue supernatant was dried in vacuo and redissolved in 3 mL of CH₃CN. The solution was layered with diethyl ether (10 mL) and kept at room temperature. Within a few days, blue crystals of **5** were obtained. The crystal crystallizes in two forms, a needle and a rectangular plate, which are manually separable. Yield: 13.3 mg, 25%. ^{1}H NMR (CD₃CN): δ 7.38 [2H, s (br), N(H)HN(H)H], 4.96 [2H, s (br), N(H)HN(H)H], 3.81 [9H, d, J_{HP} = 9.5 Hz, P(OCH_3)₃], 3.52 [9H, d, J_{HP} = 9.5 Hz, P(OCH_3)₃]. ^{31}P{^{1}H} NMR (CD₃CN): 136.0 [d, J_{PP} = 79.0 Hz, P(OCH₃)₃], 102.0 [d, J_{PP} = 79.0 Hz, P(OCH₃)₃]. Anal. Calcd for C₁₃.₂H₄₁.₈N₂.₆O₁₂Cl₂P₄Ru₂: C, 17.07; H, 4.54; N, 3.92, Found: C, 17.16; H, 4.42; N, 4.02.[33]

Reaction of Complex 4 with KO₂/18-Crown-6. In a strictly dry nitrogen atmospheric glovebox, KO₂ (8.5 mg, 0.11 mmol) was added into an acetonitrile solution (5 mL) of 18-crown-6 (60 mg, 0.23 mmol).

(32) Analytical and calculated values best matche when 0.3 molecule of CH₃CN is included.

(33) The sample subjected to analysis is a mixture of crystals crystallized with and without solvent molecules, and analytical and calculated values best match when 0.6 molecule of CH₃CN is included.

To this solution was added an acetonitrile solution (5 mL) of **4** (49.6 mg, 49.7 μmol) dropwise under agitation. The reaction mixture changed its color from green to blue in 4 h.

^{18}O₂/^{16}O₂ Mixed-Isomer Labeling Experiment. An acetonitrile solution (10 mL) of **1** (0.10 g, 0.11 mmol) was prepared in a 100 mL Schlenk flask under rigorous exclusion of air at room temperature. Mixed isotope ^{18}O₂/^{16}O₂ gas was prepared by mixing 70 mL of ^{18}O₂ and 30 mL of ^{16}O₂ in a gastight latex balloon that was connected to the manifold. After evacuation of nitrogen gas in the manifold and the flask, the mixed oxygen gas was introduced into the manifold and left undisturbed for 25 h. Products of the oxidation reaction were isolated sequentially as described above.

Supporting Information Available: Crystallographic data for the compounds in Table 8, including tables of crystal and intensity collection data, positional and thermal parameters, and interatomic distances and angles (PDF). This material is available free of charge via the Internet at http://pubs.acs.org.

JA991410U